

# Oxidation Kinetics of SPS-densified $U_3Si_2$ Fuels - Microstructure Impact

Bowen Gong<sup>1</sup>, Kun Yang<sup>1</sup>, Dong Zhao<sup>1</sup>, Andrew T. Nelson,<sup>2</sup> Jie Lian<sup>1,3,\*</sup>

<sup>1</sup> *Department of Mechanical, Aerospace & Nuclear Engineering, Rensselaer Polytechnic Institute, Troy, NY 12180,*

*USA*

<sup>2</sup> *Nuclear Fuel Development Section, Oak Ridge National Laboratory, Oak Ridge, TN 37830, USA*

<sup>3</sup> *Department of Materials Science & Engineering, Rensselaer Polytechnic Institute, Troy, NY 12180, USA*

\*Corresponding author, Email: [lianj@rpi.edu](mailto:lianj@rpi.edu); Office: 518-276-6081; Fax: 518-276-6025

## Abstract

$U_3Si_2$  is a potential candidate for accident tolerant fuels because of its high uranium density and excellent thermal conductivity in comparison to  $UO_2$ . However,  $U_3Si_2$  suffers from oxidation, steam corrosion, and subsequent disintegration/pulverization. The detailed investigation of kinetics that incorporates fundamental treatment of oxidation of  $U_3Si_2$  is scarcely reported, and the oxidation mechanisms have not been fully elucidated. In this paper, the oxidation behavior of microcrystalline (mc-) and nanocrystalline (nc-)  $U_3Si_2$  have been systematically investigated using a thermogravimetric analysis (TGA) apparatus through a series of isothermal and non-isothermal kinetic studies. The isothermal kinetic study with a model-fitting approach indicates oxidation activation energy of 85 kJ/mol for dense mc- $U_3Si_2$  and 96.4 kJ/mol for nc- $U_3Si_2$  pellets, while the isoconversional approach leads to an activation energy in the range of 70 to 85 kJ/mol for mc- $U_3Si_2$  and 75 to 86 kJ/mol for nc- $U_3Si_2$  with three most common model-free methods, including Kissinger-Akahira-Sunose, Flynn-Wall-Ozawa, and Friedman methods. The derivation of oxidation activation energies using both isothermal and isoconversional methods highlight the approach to evaluate the oxidation resistance of nuclear materials using TGA quantitatively and makes it possible to compare among various nuclear fuels.

1 **Keywords:** Oxidation kinetics, Accident tolerant fuels, Oxidation resistance,  $U_3Si_2$ , Oxidation  
2 activation energy

### 3 **1. Introduction**

4  $U_3Si_2$  has received attention in recent years as a potential candidate for accident tolerant fuels  
5 (ATFs) to replace the traditional  $UO_2$  to improve the safety margin of the light-water nuclear  
6 reactors. The major merits of  $U_3Si_2$  include higher fissile element density and improved thermal  
7 conductivity, especially at elevated temperatures.  $U_3Si_2$  has a 17% higher uranium density  
8 compared to  $UO_2$ <sup>1</sup>, which will improve the fuel content without increasing the  $U^{235}$  enrichment<sup>2</sup>.  
9  $UO_2$  is known to have a low thermal conductivity, particularly at higher temperatures, which is  
10 further reduced upon burnup during reactor operation. The inferior thermal transport behavior of  
11  $UO_2$  fuels challenges many aspects of steady-state operation and accident behavior, given the  
12 importance of efficiently heat removal from the fuel matrices to the coolant in nuclear reactor  
13 design and operation.  $U_3Si_2$  has a much higher thermal conductivity and better heat transfer  
14 efficiency at elevated temperatures<sup>3</sup>, which will be beneficial in reducing the centerline  
15 temperature<sup>4</sup>. Reduced temperature gradients in the fuel are also hypothesized to mitigate the  
16 fracture/fragmentation likely experienced during the transient conditions<sup>5</sup>. On the other hand,  
17  $U_3Si_2$  is very sensitive to oxidation and will easily pulverize if subjected to oxidizing atmospheres  
18 at elevated temperatures. Thus, oxidation resistance is a key material property to be evaluated for  
19 the overall fuel performance assessment.

20 The importance of understanding oxidation behavior in advancing  $U_3Si_2$  for use in light water  
21 reactors has motivated numerous investigations in recent years. Our previous work<sup>3</sup> has shown  
22 that monolithic  $U_3Si_2$  pellets densified by spark plasma sintering (SPS) have an improved  
23 oxidation resistance in ambient conditions, especially for the microstructure dominated by nano-

1 sized grains. Both the microcrystalline (referred to as mc- hereafter) and the nanocrystalline  
2 (referred to as nc- hereafter)  $U_3Si_2$  pellets display higher onset temperatures for oxidation over 500  
3 °C, and the dense nanostructured pellets possess reduced oxidation with extended durations  
4 required for complete oxidation. This was attributed to the effect of the strain that was introduced  
5 during the SPS sintering process. Wood *et al.* <sup>6</sup> studied the oxidation of  $U_3Si_2$  at temperatures  
6 below and above the onset temperature of oxidation (384 °C). Below the onset temperature of  
7 oxidation, a logistic curve can be used to fit the oxidation data, suggesting a two-step oxidation  
8 process from  $UO_2$  to  $U_3O_7/U_4O_9$  and then to  $U_3O_8$ . The authors also showed that the oxidation of  
9 the U element would dominate the early stage of oxidation, and Si will not be oxidized prior to the  
10 complete oxidation of U to  $UO_2$ . Harrison *et al.* <sup>7</sup> studied the oxidation mechanism of  $U_3Si_2$ , and  
11 the authors found a mix of  $USi_3$ ,  $UO_2$ , and  $U_3O_8$ . In a relevant study <sup>8</sup> regarding the initial oxidation  
12 behavior of  $U_3Si_2$ , the possible oxidation products,  $UO_2$  and uranium silicate, were identified at  
13 the early stage of oxidation.

14 In addition to monolithic  $U_3Si_2$ ,  $U_3Si_2$  composites incorporated with different additives were  
15 also designed in order to improve their oxidation and corrosion resistance <sup>9-11</sup>. Mohamad *et al.*  
16 evaluated aluminum-doped  $U_3Si_2$  and 3Y-TZP doped  $U_3Si_2$  to explore the doping effects on their  
17 oxidation resistance <sup>9,10</sup>. The authors tested the oxidation behavior of multiple specimens with  
18 various combinations of Al incorporation and  $U_3Si_2$  grain sizes. It was found that the samples with  
19 minimal addition of 1.8 at% Al were adequate to improve the oxidation onset temperature to 550  
20 °C, and iso-thermal annealing below the oxidation onset temperature in air was also adopted in  
21 order to form an oxide layer and further improve the oxidation resistance. For the 3Y-TZP doped  
22  $U_3Si_2$ , even a small amount of 3Y-TZP can significantly enhance the onset temperature (e.g., over  
23 550 °C for the 3 vol% addition of 3Y-TZP). Wood *et al.* <sup>11</sup> also studied the effect of aluminum

1 addition and confirmed that Al could delay the onset temperature and enhance the oxidation  
2 resistance. The oxidation of  $U_3Si_2$  in steam is also of great interest because, under extreme  
3 conditions, such as the cladding failure, nuclear fuels will contact and react with coolant water.  
4 Monolithic  $U_3Si_2$  can retain its integrity in 350 °C steam for over 6 hours but pulverize at 375 and  
5 400 °C <sup>12</sup>. The authors also noticed that in 6%  $H_2$  in the environment,  $U_3Si_2$  displayed a much worse  
6 performance and lost its integrity quickly at all testing temperatures. During the oxidation of  $U_3Si_2$   
7 in an atmosphere containing water, hydrogen will be produced as a byproduct, which will likely  
8 participate in other reactions and produce a ternary phase  $U_3Si_2H_{1.8}$  <sup>12,13</sup>.  $U_3Si_2$  was found to have  
9 a worse performance when hydrogen was presented in the atmosphere. Gong *et al.* <sup>14</sup> studied the  
10 Cr doped  $U_3Si_2$  and found that the Cr doping significantly enhanced the oxidation resistance of  
11  $U_3Si_2$  fuels under steam environments. Specifically, the oxidation onset temperature of 5 wt% Cr  
12 doped  $U_3Si_2$  and 10 wt% Cr doped  $U_3Si_2$  can be delayed to 520 °C in the steam ramping test, and  
13 the 10 wt% Cr doped  $U_3Si_2$  specimen can last for at least 24 hours in the 360 °C steam environment  
14 without weight change, structural disintegration, or pulverization.

15 Most studies of  $U_3Si_2$  oxidation performed for feasibility assessment have focused on  
16 identifying general behaviors, onset temperatures for rapid oxidation (ignition), and pulverization  
17 conditions as outlined above. However, a fundamental treatment of oxidation kinetics of the  $U_3Si_2$   
18 system is absent from the literature. This gap prevents contextualization of changes in oxidation  
19 behavior resulting from perturbations to processing and microstructure, use of chemical dopants,  
20 or following incorporation of fission products or other in-pile evolutions experienced during  
21 reactor operation. The kinetic study has been widely used to investigate material decomposition  
22 kinetics of organic structural materials, such as the decomposition of calcium carbonate <sup>15</sup>, woods  
23 <sup>16,17</sup>, UN <sup>18</sup>, crystallization of glass <sup>19</sup>, as well as the oxidation of  $UO_2$  <sup>20</sup>, etc. The assessment of

1 types of reactions and the determination of key kinetic parameters, e.g., the activation energy for  
2 oxidation, can be generally categorized into model-fitting methods and model-free methods. The  
3 model-fitting method fits the data of conversion  $\alpha$  and time  $t$  with a series of different models, and  
4 the one with the highest coefficient of determination ( $R^2$ ) would be selected to represent the type  
5 of reactions. Subsequently, the activation energy  $E_a$  can be derived directly from the model.  
6 Although model-fitting methods have been widely used, there are some drawbacks. Particularly,  
7 the reaction model type, such as the nucleation and growth models, diffusion models, and reaction-  
8 order models <sup>21</sup>, cannot be uniquely determined <sup>22</sup>. On the other hand, the activation energy  $E_a$  can  
9 be determined without knowing the reaction model for the model-free approach.

10 In this work, mc- and nc-  $U_3Si_2$  pellets were manufactured with SPS, and their isothermal and  
11 non-isothermal oxidation behaviors were studied by oxidation testing using TGA. The oxidation  
12 behavior was systematically assessed, and the intermediate oxidation products of  $U_3Si_2$  during the  
13 tests were collected and characterized. The TGA data were further analyzed with model-fitting and  
14 model-free approaches to evaluate the activation energy for oxidation of the  $U_3Si_2$  with different  
15 grain sizes. The results from different approaches and methods were summarized and compared  
16 with each other and also compared with the data of other common nuclear fuel materials such as  
17  $UO_2$  and UN found in the literature.

18

## 19 **2. Experimental Details**

### 20 **2.1 Sample Preparation**

21 Powders of  $U_3Si_2$  were manufactured at Idaho National Laboratory through a series of powder  
22 metallurgy processes, and the detailed fabrication process was documented in a previous study <sup>23</sup>.  
23 The grain size of the as-received powders was reduced through a high-energy ball milling (HEBM)  
24 apparatus to improve the sinterability of the powders <sup>3</sup>. A typical ball milling cycle consists of 15

1 min running time and 10 min idle time. Mc-U<sub>3</sub>Si<sub>2</sub> pellets were densified from powder ball milled  
2 for 4 cycles, while nc-U<sub>3</sub>Si<sub>2</sub> pellets were densified from powder ball milled for 44 cycles. Dense  
3 mc- and nc-U<sub>3</sub>Si<sub>2</sub> pellets used in the current work were sintered by SPS at 1000 °C for 5 mins, and  
4 all of the specimens have a density higher than 95% theoretical density. The characterization and  
5 thermomechanical properties of the samples used here can be found in literature <sup>3</sup>.

## 6 **2.2 TGA Testing for mc- and nc-U<sub>3</sub>Si<sub>2</sub> Specimens**

7 The apparatus used for oxidation kinetic study is a simultaneous DSC/TGA system (SDT650,  
8 TA instruments, DE, USA), which uses horizontal dual beams to allow continuous mass and heat  
9 flow measurements. Prior to the testing, the temperature measurement accuracy of the apparatus  
10 was calibrated with the melting point of zinc. For each run, 20 ~ 30 mg specimen was prepared  
11 and loaded into the alumina crucible. An alumina lid was also used in the test to avoid mass loss  
12 induced by blast during the oxidation process. All tests were performed in synthetic air with a flow  
13 rate of 100 ml/min. For isothermal testing, the first stage of the experiment was a ramp with a  
14 heating rate of 10 °C/min, and the second stage began when the temperature reached the target,  
15 and the sample was isothermally annealed until complete oxidation was reached. The isothermal  
16 temperatures for mc- specimens were 450, 500, and 550 °C, and temperatures for nc- specimens  
17 were 500, 550, and 600 °C. The duration of the oxidation process of mc-specimen at 600 °C was  
18 too short due to its faster oxidation kinetics; thus, a lower range of temperatures was adopted for  
19 the oxidation kinetic study of mc-specimens.

## 20 **2.3 Deriving the Activation Energy using Isothermal Methods**

21 For solid-state reactions, it was reported <sup>24</sup> that the reaction kinetics could be described by  
22 formula (1), where  $\alpha$  is the conversion representing the fraction that has been reacted,  $t$  is time,  $k$   
23 is the reaction rate that can be exponentially represented in the Arrhenius form (2) <sup>25-27</sup>, and  $f(\alpha)$

1 is the reaction model depicting the type of reactions. In formula (2),  $k_0$  is a pre-exponential factor,  
 2  $E_a$  is the activation energy,  $R$  is the gas constant, and  $T$  is the temperature in the unit of  $K$ .  
 3 Conversion  $\alpha$  can be calculated through equation (3) based on 17% weight gain when uranium  
 4 was fully oxidized to  $U_3O_8$ . An additional 8 wt% gain is expected as Si is further oxidized to  $SiO_2$   
 5 with slower oxidation kinetics. Therefore, only the full oxidation reaction of U is considered based  
 6 on the 17 wt% gain for the analysis of their oxidation kinetics since the initial rapid oxidation is  
 7 mainly dominated by the oxidation of  $U_3Si_2$  to  $UO_2$  and then the oxidation of  $UO_2$  to  $U_3O_8$ , which  
 8 will be discussed later. In equation (3),  $W_i$ ,  $W_t$ , and  $W_f$  are initial, actual, and final weight,  
 9 respectively, all of which were measured during the oxidation process <sup>26</sup>.

10

$$11 \quad \frac{d\alpha}{dt} = kf(\alpha) \#(1)$$

12

$$13 \quad k = k_0 \exp\left(-\frac{E_a}{RT}\right) \#(2)$$

14

$$15 \quad \alpha = \frac{W_i - W_t}{W_i - W_f} \#(3)$$

16

17 According to Hancock <sup>28</sup>, the reaction kinetics that is associated with nucleation and grain  
 18 growth can be generally expressed in formula (4) or its logarithm form (5), where  $B$  is a constant  
 19 related to the nucleation and grain growth and  $n$  is a characteristic value. It was also mentioned in  
 20 <sup>28</sup> that two Avrami-Erofeev equations (also referred to as Johnson-Mehl-Avrami-Erofeev-  
 21 Kholmogorov equation) and one first-order formula could lead to the linear relationship between  
 22  $\ln[-\ln(1-\alpha)]$  and  $\ln(t)$ . The values of the characteristic factor  $n$  were determined through the data  
 23 fitting with Avrami-Erofeev equations. The equations (4) and (5) are based on the assumptions  
 24 that nucleation happens with randomness, and when nuclei grow and collide with each other, the

1 growth will terminate <sup>29-31</sup>. The value of  $n$  can be determined based on the slope of the term  
 2  $\ln[ -\ln(1 - \alpha) ]$  and  $\ln t$ . For common solid-state rate expressions (see partial list in the Table I),  
 3 the oxidation reactions can be classified in one of the model groups, such as the nucleation model,  
 4 geometrical contraction model, diffusion model, as well as reaction-order model <sup>21</sup>.

5 Combining formula (1) and (2), equation (6) <sup>21</sup> can be obtained, which can be further expressed  
 6 as its integration form shown in formula (7), where  $g(\alpha)$  corresponds to the integrated reaction  
 7 form that is a counterpart of  $f(\alpha)$  (see Table I <sup>32</sup>). For the listed models, A represents for Avarami-  
 8 Erofeev model, with the number after A representing the factor in the differential form; the same  
 9 goes for the models starting with R and D, which represent geometrical contraction models and  
 10 diffusion models, respectively; and F represents for reaction-order models, and the number after F  
 11 represents for the corresponding order.

12 By plotting the corresponding  $g(\alpha)$  with time  $t$ , a series of values of slope  $k$  can be obtained,  
 13 and  $g(\alpha)$  corresponding to different reaction models are summarized in the Table I. The activation  
 14 energy  $E_a$  can be subsequently derived through plotting  $\ln k$  against  $1/T$  based on equation (2), and  
 15 the slope gives the value of the  $E_a$ .  $E_a$  can be assumed to remain the same in the calculation for the  
 16 sake of simplicity.

17  
 18 
$$\alpha = 1 - \exp(-B t^n) \#(4)$$

19  
 20 
$$\ln[ -\ln(1 - \alpha) ] = \ln B + n \ln t \#(5)$$

21  
 22 
$$\frac{d\alpha}{dt} = A \exp\left(-\frac{E_a}{RT}\right) f(\alpha) \#(6)$$

23  
 24 
$$g(\alpha) = A \exp\left(-\frac{E_a}{RT}\right) t \#(7)$$

25 **Table I: Partial list of common solid-state reaction models**

Model	Description	Kinetic equation (differential, $f(\alpha)$ )	Kinetic equation (integral, $g(\alpha)$ )	n
-------	-------------	--	--	---

A2	Nucleation	$2(1 - \alpha)[ - \ln(1 - \alpha)]^{\frac{1}{2}}$	$[ - \ln(1 - \alpha)]^{\frac{1}{2}}$	2
A3	Nucleation	$3(1 - \alpha)[ - \ln(1 - \alpha)]^{\frac{2}{3}}$	$[ - \ln(1 - \alpha)]^{\frac{1}{3}}$	3
R2	Geometrical contraction	$2(1 - \alpha)^{\frac{1}{2}}$	$1 - (1 - \alpha)^{\frac{1}{2}}$	1.11
R3	Geometrical contraction	$3(1 - \alpha)^{\frac{1}{2}}$	$1 - (1 - \alpha)^{\frac{1}{3}}$	1.07
D1	Diffusion	$\frac{1}{2\alpha}$	$\alpha^2$	0.62
F0	Reaction-order	1	$\alpha$	1.24
F1	Reaction-order	$1 - \alpha$	$ - \ln(1 - \alpha)$	1

1

## 2 2.4 Deriving the Activation Energy using Isoconversional Methods

3 For non-isothermal testing, various heating rates were adopted during the thermogravimetric  
4 analysis, ranging from 2 °C/min to 15 °C/min. The temperature range during the test was from  
5 room temperature to 1000 °C for each experiment. For the oxidation process with heating rate  $\beta$ ,  
6 the temperature can be written as a function of time, as in equation (8) below, where  $T$  is the  
7 temperature at time  $t$ ,  $T_i$  is the initial temperature. Taking the derivative of equation (8) with respect  
8 to variable  $t$ , equation (9) can be obtained. Combining with equation (2) and the kinetic equation  
9 (10), the fundamental equation for non-isothermal analysis can be obtained, as shown in equation  
10 (11). The detailed derivation process can be found in <sup>33</sup> as well. Based on different reaction models  
11 (see Table 1), several isoconversional methods have been derived, including Kissinger-Akahira-  
12 Sunose (KAS) method in equation (12), Flynn-Wall-Ozawa (FWO) method <sup>34,35</sup> in equation (13),  
13 and Friedman method <sup>36</sup> in equation (14), etc. These three isoconversional methods will be  
14 primarily considered in this work to derive the activation energy. Therefore, by plotting the  
15 corresponding left-hand-side term of equations (12), (13), and (14) with respect to  $1000/T$  at each  
16 value of the conversion  $\alpha$ , the activation energies,  $E_a$ , can be obtained from the slopes of a series  
17 of straight lines. The FWO method was independently proposed by Flynn and Wall <sup>35</sup>, and Ozawa  
18 <sup>34</sup> in the 1960s, in which the relationship between the temperature at each conversion and the  
19 heating rate was found to be related to the activation energy. Similarly, the Friedman method <sup>36</sup>

1 depicts the relationship between the conversion rate and the rate constant for the n-th order reaction.  
 2 On the other hand, another relationship was found between heating rate and temperature at a given  
 3 conversion, laying the foundation of the KAS method <sup>37,38</sup>. In Ozawa's paper comparing these  
 4 three methods, it was also shown that all these three isoconversional methods could be derived  
 5 from the same foundational equation. The derivation was documented thoroughly in <sup>37</sup> and will  
 6 not be elaborated here. However, the FWO method was believed to be more accurate than the KAS  
 7 method due to the more accurate approximation in the former.

8

$$9 \quad T = T_i + \beta t \#(8)$$

$$10 \quad \frac{dT}{dt} = \beta \#(9)$$

$$11 \quad \frac{d\alpha}{dt} = kf(\alpha) \#(10)$$

$$12 \quad \frac{d\alpha}{dT} = \frac{k_0}{\beta} \exp\left(-\frac{E_a}{RT}\right) f(\alpha) \#(11)$$

$$13 \quad \ln \frac{\beta}{T^2} = \ln \frac{AR}{E_a g(\alpha)} - \frac{E_a}{RT} \#(12)$$

$$14 \quad \ln \beta = \ln \frac{AE_a}{Rg(\alpha)} - 5.331 - \frac{1.052E_a}{RT} \#(13)$$

$$15 \quad \ln \left(\frac{d\alpha}{dt}\right) = \ln[Af(\alpha)] - \frac{E_a}{RT} \#(14)$$

16

## 17 **2.5 Microstructural Characterization of the Intermediate Products**

18 To study the oxidation mechanisms, each sample was heated up in the TGA chamber with a  
 19 heating rate of 10 °C/min until the desired weight gain was achieved. Then, the TGA program was  
 20 terminated immediately, and the inflow gas was immediately switched to high purity Ar to prevent  
 21 further oxidation. After cooling down, the residual was manually ground for characterization.  
 22 Intermediate oxidizing products were obtained at five weight gains, including 5%, 10%, 15%, 18%,  
 23 and 21%. The residuals were collected, ground, and were then characterized with XRD patterns,

1 which were obtained from an X'Pert XRD system (Westborough, Massachusetts) with Cu K $\alpha$   
2 irradiation. The wavelength was set to 1.5406 Å. The scanning range is from 20° to 80°, and the  
3 scanning step is 0.05°. The scanning rate is ~2 s/step.

4

### 5 **3. Results and Discussion**

#### 6 **3.1 Isothermal Oxidation Behavior of SPS-sintered U<sub>3</sub>Si<sub>2</sub>**

7 A set of representative TGA data were plotted in Fig. 1, which was obtained from isothermal  
8 annealing at 500 °C for both mc- and nc-specimens. Both mc- and nc-specimens display initial  
9 rapid weight gains up to 17 wt% corresponding to oxidation of U<sub>3</sub>Si<sub>2</sub> to U<sub>3</sub>O<sub>8</sub>, and the final weight  
10 gain of both samples is close to 21%, matching with results of ramping tests in the literature <sup>3,11</sup>.  
11 It is expected that further oxidation of Si up to 24.9 wt% will occur at a much lower oxidation rate.  
12 Note that full oxidation of 24.9 wt% was not reached, suggesting residual unreacted silicon in both  
13 specimens). The initial rapid weight gain attributed to the oxidation of U<sub>3</sub>Si<sub>2</sub> is evidenced by the  
14 XRD diffraction of the powders subjected to intermediate oxidation steps showing the formation  
15 of UO<sub>2</sub> at 5 wt% gain sample and the appearance of U<sub>3</sub>O<sub>8</sub> in the 10 wt% gain sample, which are  
16 discussed in next section). It is observed that grain structure impacts oxidation kinetics  
17 significantly. Oxidation initiates more rapidly in the mc-specimen than in the nc-specimen, as  
18 evidenced by the delayed onset temperature for the nc-specimen. Additionally, nc-specimen takes  
19 slightly longer time to reach full oxidation, indicating a better oxidation resistance. This was also  
20 confirmed in the ramping tests from earlier work <sup>3</sup> and was attributed to the residual strain induced  
21 from the SPS sintering process, in which a compressive strain experienced in the nc-U<sub>3</sub>Si<sub>2</sub> matrices  
22 may be beneficial to preventing the initiation and propagation of micro-cracks in the oxidation  
23 scale resulting from the vigorous exothermic heat release and thermal stress. Upon strain relaxation

1 of the SPS densified pellets either by post-sintering annealing or fragmentation, the onset  
2 temperature of the nc- $U_3Si_2$  decreased accordingly, confirming the impact of the strain engineering  
3 and microstructure control on the oxidation kinetics of  $U_3Si_2$ .

### 4 **3.2 Intermediate Products During the Oxidation Process**

5 To further understand the oxidation process and reaction type, intermediate products with  
6 targeted weight gains are obtained, and their oxidation products were characterized. Fig. 2 shows  
7 the XRD patterns of intermediate products during the oxidation process of mc- $U_3Si_2$  from the  
8 sample with 5% weight gain up to 18%, along with the XRD patterns of the as-sintered  $UO_2$  and  
9  $U_3Si_2$  for reference. It can be noticed that when there is 5% weight gain, the phases of  $UO_2$  and  
10  $U_3Si_2$  can be identified, indicating that the rapid oxidation is attributed to the oxidation of  $U_3Si_2$  to  
11  $UO_2$ . Multiple steps of oxidation from  $U_3Si_2$  to  $USi_3$  and  $USi_3$  to  $UO_2$  may occur, as reported by a  
12 previous study by Wood et al. <sup>6</sup>, in which  $USi_3$  was identified as an intermediate product.  $USi_3$  was  
13 also observed in this work based on the XRD data, confirming the validity of the proposed  
14 reactions in literature <sup>6</sup>. When  $U_3Si_2$  is further oxidized to 10% weight gain, the  $UO_2$  phase  
15 dominates, and only minor  $U_3Si_2$  can be observed. At the same time,  $U_3O_8$  peaks appear in the  
16 XRD pattern. When weight gain reaches 15%, the peaks of  $U_3Si_2$  can be barely seen, suggesting  
17 that almost all of the  $U_3Si_2$  are fully oxidized. The majority of peaks can be indexed to  $UO_2$  and  
18  $U_3O_8$ . Finally, at 18% weight gain, all peaks can be indexed to  $U_3O_8$ , indicating that all of the  
19 uranium has been oxidized to  $U_3O_8$ . These results confirmed that the oxidation of  $U_3Si_2$  consists  
20 of two major steps: the oxidation of  $U_3Si_2$  to  $UO_2$  and the oxidation of  $UO_2$  to  $U_3O_8$ , where the  
21 second step may be initiated simultaneously before the completion of the first reaction.

22 In a study of the oxidation mechanism of  $U_3Si_2$  <sup>7</sup>, the authors conducted thermodynamic  
23 calculations based on the Gibbs free energy and concluded that  $UO_2$  would form before the  
24 formation of  $SiO_2$  due to its higher stability. After this, the oxidation from Si to  $SiO_2$  was reported

1 to be thermodynamically favorable than the further oxidation of  $\text{UO}_2$  to  $\text{U}_3\text{O}_8$ . However, it has  
2 been found that during the isothermal oxidation of  $\text{U}_3\text{Si}_2$ , the primary oxidation products are  $\text{UO}_2$   
3 and  $\text{USi}_3$  <sup>6</sup>, instead of  $\text{SiO}_2$ . Si was believed to be protected by the oxidation layer of  $\text{UO}_2$ , such  
4 that  $\text{UO}_2$  will react with oxygen before Si and thus get oxidized before Si. TEM images in <sup>7</sup> also  
5 indicated that Si was surrounded by nc-  $\text{U}_3\text{O}_8$ , confirming the protection of  $\text{UO}_2$  to the oxidation  
6 of Si. The volumetric expansion from  $\text{U}_3\text{Si}_2$  to  $\text{UO}_2$  was estimated to be ~17%, followed by another  
7 36% volumetric expansion from  $\text{UO}_2$  to  $\text{U}_3\text{O}_8$ . The strain introduced during this process, as well  
8 as the formation of the nanograins, was believed to be the intrinsic drive force for the pulverization  
9 of the pellet <sup>7</sup>.

10

### 11 **3.3 Deriving the Activation Energy Based on the 17% Weight Gain for mc- and nc- $\text{U}_3\text{Si}_2$**

12 The activation energies derived are based on 17% weight gain assuming all of the  $\text{U}_3\text{Si}_2$  has  
13 been fully oxidized to  $\text{U}_3\text{O}_8$  and can be used to assess the oxidation resistance of  $\text{U}_3\text{Si}_2$  fuels. Note  
14 that oxidation of  $\text{UO}_2$  to  $\text{U}_3\text{O}_8$  also occurs, accompanied by the oxidation of  $\text{U}_3\text{Si}_2$ , as shown later  
15 by phase analysis of the intermediate oxidation stage. However,  $\text{U}_3\text{Si}_2$  displays much lower  
16 activation energy than  $\text{UO}_2$ , and thus, its much faster oxidation kinetics dominates the initial rapid  
17 weight gain. Fig. 3 shows the plots of  $\ln[-\ln(1-\alpha)]$  versus  $\ln t$  according to equation (5). The  
18 linear relationship is apparent at all three temperatures for both mc- and nc- specimens. The  
19 characteristic value  $n$  can be derived from the slope of the linear plot and can be associated with  
20 different solid-state reaction mechanisms (Table I). Some of the common reactions and their  
21 corresponding characteristic values are listed as well <sup>21,24,28</sup>.

22 For the kinetic analysis of the TGA data, it was reported <sup>24</sup> that several different methods could  
23 be used. The first method is to calculate the reduced time  $t/t_{0.5}$  and compare it with the  
24 characteristics of well-known reaction models shown in the Table I. The drawback was that the

1 reduced time was similar to each other for different reaction models, and thus it would be hard to  
2 distinguish among various models. Another method was to derive the characteristic value  $n$  and  
3 compare it to the value of  $n$  in the Table I for known reactions and determine the reaction model.  
4 For mc-U<sub>3</sub>Si<sub>2</sub>,  $n$  was found to be 1.24 at 450 °C, denoting zero-order kinetics; at 500 °C,  $n$  was  
5 found to be 1.43, denoting a transition from decomposition controlling mechanism to nucleation;  
6 at 550 °C,  $n$  was found to be 2.5, which implies a nucleation model between A<sub>2</sub> and A<sub>3</sub>,  
7 corresponding to bi-dimensional and three-dimensional nucleation and growth models. For nc-  
8 U<sub>3</sub>Si<sub>2</sub>,  $n$  was found to be 2.67, 3.66, and 2.2 for nc-specimen at 500, 550, and 600 °C. Although  
9 the values of reaction order  $n$  are different at different temperatures, they are all in the range of 1.2  
10 to 3.6, suggesting that the mechanisms at these temperatures are all controlled by the nucleation  
11 and growth process. It was reported in <sup>20</sup> that the occurrence of nucleation and growth at the same  
12 time makes it challenging to analyze the detailed mechanism of each. The proposed practical  
13 analysis for the solid-gas reaction <sup>39</sup> is to treat the reactant as spherical particles with a uniform  
14 size. Nuclei randomly form on the particles' surface with nucleation rate in proportion to the  
15 unreacted surface. The growth rate of nuclei is constant in all directions. The authors in <sup>20</sup> further  
16 assumed that only one nucleus forms on one particle at low temperatures and claimed that the  
17 reaction would follow first-order kinetics controlled by nucleation. At elevated temperatures, the  
18 growth process becomes dominant, and the reaction curve would deviate from the first-order  
19 reaction and gradually approach the sigmoid shape. Boase <sup>40</sup> also studied the oxidation of  
20 unirradiated UO<sub>2</sub> pellets between 320 to 460 °C and also obtained a series of varying values of  $n$ ,  
21 suggesting a non-isokinetic process during which the nucleation and growth rate change.

22 Another commonly adopted method to determine the reaction model involves fitting the  
23 conversion  $\alpha$  and time  $t$  with various reaction models, and the model with the highest correlation

1 coefficient  $R^2$  will be used to represent the reaction <sup>24</sup>. After fitting the values of  $\alpha$  and time  $t$  with  
 2 possible models, the best models with the highest  $R^2$  for mc- and nc- specimens are listed in the  
 3 Table II, along with their corresponding  $R^2$  fitting. The models that best fit the data for mc- $U_3Si_2$   
 4 are model  $A_2$  at 450 and 500 °C, and model  $A_3$  at 550 °C. The best models for nc-specimens are  
 5 model  $A_3$  at 500 and 550 °C, and model  $A_2$  at 600 °C. The  $R^2$  of these models with the best fit are  
 6 listed in the Table II, from which it was found that the oxidation of mc- and nc- $U_3Si_2$  can generally  
 7 be fitted with the Avrami–Erofeev model with slight variation in the reaction order.

8 **Table II: The top two best model fitting for two samples at three different temperatures**

Sample	Temperature (°C)	Model	$R^2$
mc- $U_3Si_2$	450	$A_2$	0.952
mc- $U_3Si_2$	500	$A_2$	0.988
mc- $U_3Si_2$	550	$A_3$	0.977
nc- $U_3Si_2$	500	$A_3$	0.993
nc- $U_3Si_2$	550	$A_3$	0.973
nc- $U_3Si_2$	600	$A_2$	0.969

9

10 The following analysis is based on the model with the highest  $R^2$  listed in the Table II as there  
 11 might be slight variations in the derived activation energy if other models were selected. Fig. 4A  
 12 and 4D present the variation of conversion  $\alpha$  with time for both mc- $U_3Si_2$  and nc- $U_3Si_2$  specimens,  
 13 respectively, along with the fitted curve. The reaction curves for both mc- $U_3Si_2$  and nc- $U_3Si_2$   
 14 display a sigmoid shape, which corresponds to the nucleation/growth kinetics. In a review  
 15 regarding the oxidation of  $UO_2$  <sup>41</sup>, the authors introduced the detailed stepwise oxidation of  $UO_2$ ,  
 16 which consists of two reactions. The first reaction produces  $U_3O_7/U_4O_9$ , while the second is the  
 17 further oxidation from  $U_3O_7/U_4O_9$  to  $U_3O_8$ . These two steps have different reaction mechanisms,  
 18 with the first controlled by diffusion while the second controlled by nucleation/growth. The  
 19 reaction rate of the diffusion-controlled reaction was limited by the oxidation diffusion through

1 the formed oxidation layer, and thus, the weight gain plot will show a parabolic shape <sup>41</sup>. The  
2 formation of  $U_3O_8$ , on the other hand, is controlled by the nucleation/growth mechanism, and thus,  
3 its weight gain would display a sigmoid shape. In another paper discussing the sigmoid shape  
4 observed in these curves, the authors stated that it could be attributed to the fresh reactive surface  
5 generated by macro-cracking <sup>42</sup>. The authors also discussed the detailed oxidation steps, which  
6 consisted of the initial low oxidation rate stage, followed by the second stage with the accumulation  
7 of  $UO_{2+x}$  layer and the increase of the surface volume ratio, resulting in an increased oxidation  
8 rate. The third stage is accompanied by cracking, as well as the  $U_3O_8$  nucleation and growth, and  
9 finally, the constant oxidation until complete oxidation. The authors also noted that during the step  
10 that  $U_3O_7$  was oxidized to  $U_3O_8$ , the reaction could be interpreted with a nucleation and growth  
11 mechanism.

12 For the oxidation of  $U_3Si_2$ , diffusion-controlled oxidation was not observed. The oxidation is  
13 likely dominated by the reaction controlled by the nucleation and growth mechanism. At the end  
14 of the oxidation, starting from the conversion of  $\sim 0.75$ , the fitted curve slightly deviates from the  
15 actual data points, which can be attributed to the fact that the fitting parameters were derived based  
16 on the conversion range of 0.15 to 0.5, corresponding to the oxidation from  $U_3Si_2$  to  $UO_2$  (which  
17 is confirmed from the XRD patterns in Fig. 2). When the conversion reaches  $\sim 0.75$ , all the  $U_3Si_2$   
18 has been oxidized to  $UO_2$ , and  $UO_2$  will start to be further oxidized to  $U_3O_7/U_4O_9$  and finally  $U_3O_8$ .  
19 Since the oxidation of  $UO_2$  could occur before the completion of oxidation of  $U_3Si_2$ , the fitted  
20 curve slightly underestimates the actual conversion data.

21 For all the reaction curves fitted with the Avrami-Erofeev model, the relationship between  $\alpha$   
22 and time is in a sigmoid shape. It can be noticed that the fitted curve matches very well with the  
23 original data. The corresponding values of  $k$  at each temperature were determined through the

1 linear fitting of the plot of the corresponding  $g(\alpha)$  versus time  $t$  and are shown in Fig. 4B and 4E.  
2 It can be seen that the linear lines match well with the data points, indicating an excellent fit for  
3 all of the datasets. The values of  $k$  were labeled aside each line, ranging from 0.02 to 0.13 for mc-  
4  $U_3Si_2$  and 0.02 to 0.11 for nc- $U_3Si_2$ . Fig. 4C and 4F show the fitting of  $\ln k$  vs.  $1000/T$ , which  
5 also shows excellent linearity. The activation energy of mc-specimens and nc-specimens can be  
6 determined to be  $85 \pm 12$  kJ/mol and  $96.4 \pm 8$  kJ/mol with an  $R^2$  of 0.97 and 0.99, respectively.  
7 The uncertainty in activation energy was calculated based on the uncertainty in the slope. The nc-  
8  $U_3Si_2$  specimen displays slightly higher activation energy compared to its mc- $U_3Si_2$  counterpart,  
9 suggesting that nc- $U_3Si_2$  may have an improved oxidation resistance during the oxidation. This  
10 matches with the findings from Fig. 1 that nc- $U_3Si_2$  has an extended onset temperature compared  
11 to the mc- $U_3Si_2$  counterpart, although reaction theory<sup>43</sup> predicts that the reaction rate will increase  
12 when grain size decreases due to greater surface per unit mass available for the nucleation with  
13 smaller particle size. It was reported<sup>42</sup> that at the later stage of the  $UO_2$  oxidation, starting from  $\alpha$   
14  $\approx 0.5$ , the oxidation rate is much lower for nc- $UO_2$  than mc- $UO_2$ , which is also contrary to the  
15 expectation and was attributed to the fact that nc- $UO_2$  was more difficult to crack during the  
16 oxidation process. The authors in<sup>41</sup> stated that  $UO_2$  with sub-micron grains might have better  
17 resistance to the cracking induced from volume expansion as that tensile strains are proportional  
18 to grain size. This is consistent with our observation of enhanced oxidation resistance for nc- $U_3Si_2$   
19 than mc- $U_3Si_2$ , in which the strong compressive strain field induced in SPS densified nc- $U_3Si_2$   
20 pellet may be beneficial to prevent microcrack formation and propagation.

### 21 3.4 Deriving the Activation Energy of mc- $U_3Si_2$ and nc- $U_3Si_2$ From Isoconversional Methods

22 Fig. 5 shows the weight change of the mc- $U_3Si_2$  and nc- $U_3Si_2$  specimens during non-isothermal  
23 TGA tests with various heating rates, including 2 °C/min, 5 °C/min, and 10 °C/min. For both

1 samples, increasing the heating rate from 2 °C/min to 10 °C/min generally leads to a  
 2 thermogravimetric (TG) curve shifting towards higher temperature without any significant shape  
 3 changes. Similar findings were reported in <sup>35,44-46</sup>, and it was explained that heat transfer was  
 4 inefficient at higher temperatures.

5 For both specimens, the activation energies,  $E_a$ , are further evaluated and determined by three  
 6 isoconversional methods, i.e., KAS, FWO, and Friedman. The plots of  $\ln \frac{\beta}{T^2}$  and  $1000/T$  applying  
 7 the KAS method are shown in Figs. 6A and 6D for mc-U<sub>3</sub>Si<sub>2</sub> and nc-U<sub>3</sub>Si<sub>2</sub> specimens, respectively.  
 8 The data at each conversion  $\alpha$  can be fitted with a straight line. The average  $E_a$  derived from the  
 9 KAS method is determined to be  $70.3 \pm 5.9$  kJ/mol for mc-U<sub>3</sub>Si<sub>2</sub> and  $75.8 \pm 3.8$  kJ/mol for nc-  
 10 U<sub>3</sub>Si<sub>2</sub>. Figs. 5B and 5E show the plots of  $\ln \beta$  vs.  $1000/T$ , which also show a similar linear  
 11 relationship as in Figs. 6A and 6D. The average  $E_a$  derived from the FWO method is estimated to  
 12 be  $79.2 \pm 6$  kJ/mol for mc-U<sub>3</sub>Si<sub>2</sub> and  $89.6 \pm 3.8$  kJ/mol for nc-U<sub>3</sub>Si<sub>2</sub>. Figs. 6C and 6F show the  
 13 plots of  $\ln \left( \frac{d\alpha}{dt} \right)$  vs.  $1000/T$ , suggesting that the average  $E_a$  derived using Friedman's method is  
 14 around  $85.3 \pm 13$  kJ/mol for mc-U<sub>3</sub>Si<sub>2</sub> and  $86.3 \pm 9.2$  kJ/mol for nc-U<sub>3</sub>Si<sub>2</sub>. As aforementioned, the  
 15 uncertainty in activation energy was calculated based on the uncertainty in the slope. The  
 16 activation energies derived for both samples are summarized in the Table III below. The variation  
 17 of activation energy might be partly attributed to the claim that activation energy is dependent on  
 18 the physical condition of the sample <sup>47</sup>, which is still under debate <sup>42</sup>.

19

20 **Table III: Summary of activation energies of mc-U<sub>3</sub>Si<sub>2</sub> and nc-U<sub>3</sub>Si<sub>2</sub> with 3 isoconversional**  
 21 **model-free methods**

Sample	$E_a$ (kJ/mol)		
	KAS	FWO	Friedman
mc-U <sub>3</sub> Si <sub>2</sub>	$70.3 \pm 5.9$	$79.2 \pm 6$	$85.3 \pm 13$
nc-U <sub>3</sub> Si <sub>2</sub>	$75.8 \pm 3.8$	$89.6 \pm 3.8$	$86.3 \pm 9.2$

1  
2  
3  
4  
5  
6  
7  
8  
9  
10  
11  
12  
13  
14  
15  
16  
17  
18  
19  
20  
21  
22  
23  
24

### 3.5 Activation Energy for Oxidation and Comparison with other Nuclear Fuels

It can be noticed that the activation energy derived from all three methods is in general consistent with each other, suggesting a valid derivation and sound determination of activation energies using various methods. Compared to the activation energy derived from the isothermal kinetic study previously, a great agreement can also be noticed in the derived activation energies that nc-U<sub>3</sub>Si<sub>2</sub> shows slightly higher activation energies than mc-U<sub>3</sub>Si<sub>2</sub>. These results are consistent with experimentation in which the nc-U<sub>3</sub>Si<sub>2</sub> densified by SPS shows greater oxidation resistance on mc-counterpart from the delayed onset temperature for oxidation. This comparison further confirms the validity of using both isothermal and isoconversional methods to effectively analyze the oxidation process and evaluate the oxidation activation energy of nuclear fuels. Mechanistic understanding based on modeling fitting of isothermal growth kinetic data also reveals a dominant nucleation and growth mechanism responsible for the rapid oxidation stage of the U<sub>3</sub>Si<sub>2</sub> despite the challenge of differentiating nucleation and growth processes. It should also be noted that multistep oxidation may also occur for U<sub>3</sub>Si<sub>2</sub> based on thermodynamic modeling<sup>48</sup> of reactions of: (1)  $U_3Si_2 \rightarrow USi_3 + UO_2$ ; (2)  $USi_3 \rightarrow UO_2 + Si$ ; (3)  $Si \rightarrow SiO_2$  and  $UO_2 \rightarrow U_3O_8$ . The multistep oxidation of U<sub>3</sub>Si<sub>2</sub> to UO<sub>2</sub> and U<sub>3</sub>O<sub>8</sub> was evidenced by the observation of intermediate oxidation products of USi<sub>2</sub> and free Si in previous literature<sup>6,49</sup>. Different kinetics and activation energies may be expected for each oxidation reaction. In this work, no clear transition in the oxidation rate could be observed in the rapid oxidation stage up to 17 wt% that might be correlated to specific oxidation steps. In addition, our XRD analysis of intermediate oxidation products (discussed in Fig. 2) do not show the formation of observable amounts of USi<sub>3</sub> and free Si, implying the simultaneous occurrence of multiple oxidation processes. Therefore, our isothermal analysis is based on the rapid oxidation up to 17% weight gains, in which U<sub>3</sub>Si<sub>2</sub> is fully

1 oxidized to  $\text{UO}_2$ . The activation energy determined based on isothermal annealing and model  
2 fitting for both mc- and nc-specimens are apparent activation energies of rate-controlled processes  
3 for nucleation and growth instead of the energy barrier for specific oxidation reactions.

4 Ohmichi *et al.*<sup>50</sup> studied the initial-stage oxidation of UC and UN and reported an activation  
5 energy of 120 and 124 kJ/mol, respectively, higher than that of  $\text{U}_3\text{Si}_2$ . The activation energy of  
6 oxidation of  $\text{UO}_2$  to  $\text{U}_3\text{O}_7/\text{U}_4\text{O}_9$  was reported to be in the range of 90.8 kJ/mol to 120 kJ/mol based  
7 on the parabolic kinetics and 98.6 kJ/mol based on the diffusion-controlled kinetic. The oxidation  
8 activation energy of the pellet  $\text{UO}_2$  to  $\text{U}_3\text{O}_8$  was scattered in the range of 100-160 kJ/mol depending  
9 on the temperature range, sample conditions, as well as analyzing approaches<sup>41</sup>. The  
10 recommended value for activation energy for  $\text{UO}_2$  oxidation at a temperature below 325 °C,  
11 however, is given to be 154 kJ/mol. McEachern *et al.*<sup>51</sup> derived the activation energy for the  
12 formation of  $\text{U}_3\text{O}_8$  during the oxidation of  $\text{UO}_2$ , which is  $146 \pm 10$  kJ/mol. The lower activation  
13 energies for  $\text{U}_3\text{Si}_2$  than UN, UC, and  $\text{UO}_2$  suggest that  $\text{U}_3\text{Si}_2$  fuels are probably more prone to  
14 oxidation with much faster oxidation kinetics, consistent with the experimental observations  
15 shown in Fig. 1 with rapid initial oxidation from  $\text{U}_3\text{Si}_2$  to  $\text{UO}_2$ . These results also underscore the  
16 importance of further improving the oxidation resistance of  $\text{U}_3\text{Si}_2$  fuels as the leading concept of  
17 ATF fuels for potential applications.

18

#### 19 **4. Conclusions**

20 In summary, the oxidation behavior of mc- and nc- $\text{U}_3\text{Si}_2$  was evaluated with TGA through both  
21 isothermal and non-isothermal dynamic oxidation testing. Activation energies  $E_a$  of oxidation of  
22 both  $\text{U}_3\text{Si}_2$  was derived as  $85 \pm 12$  and  $96.4 \pm 8$  kJ/mol for mc- and nc- $\text{U}_3\text{Si}_2$ , respectively, with an  
23  $R^2$  of 0.97 and 0.99, based on the isothermal oxidation kinetic analysis. The activation energies

1 obtained are in the range of 70 to 85 kJ/mol for mc-U<sub>3</sub>Si<sub>2</sub> and 76 to 90 kJ/mol for nc-U<sub>3</sub>Si<sub>2</sub> using  
2 the isoconversional approaches with KAS, FWO, and Friedman methods. The results obtained  
3 from the isothermal kinetic study and the isoconversional kinetic study are in general consistent,  
4 validating the determination of the activation energies. The nc-U<sub>3</sub>Si<sub>2</sub> displays greater activation  
5 energies for oxidation than mc-U<sub>3</sub>Si<sub>2</sub> and thus improved oxidation resistance based on the slightly  
6 greater activation energy determined by multiple methods and experimentally-observed higher  
7 onset temperature for oxidation. The intermediate oxidation products were collected and  
8 characterized, and it was found that U<sub>3</sub>Si<sub>2</sub> was oxidized to UO<sub>2</sub> first and then to U<sub>3</sub>O<sub>8</sub> during the  
9 oxidation process. As the kinetics study of oxidation of nuclear fuels is very limited in the literature,  
10 this systematic investigation of U<sub>3</sub>Si<sub>2</sub> with different microstructures and determination of  
11 activation energies could be useful to further understand the behavior of U<sub>3</sub>Si<sub>2</sub> as a candidate of  
12 ATFs. These findings are supplemental to the existing knowledge of U<sub>3</sub>Si<sub>2</sub> and can be used as  
13 reference data when constructing simulation tools for nuclear performance predictions. The  
14 workflow and methodology presented here highlight the potential of using TGA to assess the  
15 oxidation resistance and determine the critical oxidation parameters of U<sub>3</sub>Si<sub>2</sub> and nuclear materials  
16 such as UO<sub>2</sub> and UN.

17

## 18 **5. Data availability**

19 The data that support the findings of this study are available from the corresponding author  
20 upon reasonable request.

21

## 22 **6. Acknowledgment**

1 This work is supported by the U.S. Department of Energy, Office of Nuclear Energy under a  
2 Nuclear Energy University Program [award number: DE-NE0008532].

3

#### 4 7. References

- 5 1 D. A. Lopes, S. Uygur, and K. Johnson, *Journal of Nuclear Science Technology* **54**, 405  
6 (2017).
- 7 2 L. H. Ortega, B. J. Blamer, J. A. Evans, and S. M. McDevitt, *Journal of Nuclear Materials*  
8 **471**, 116 (2016).
- 9 3 B. Gong, T. Yao, P. Lei, J. Harp, A. T. Nelson, and J. Lian, *Journal of Alloys Compounds*  
10 **825**, 154022 (2020).
- 11 4 K. Metzger, T. Knight, and R. Williamson, "Model of U3Si2 fuel system using BISON fuel  
12 code," (2014).
- 13 5 U. Carvajal-Nunez, T. A. Saleh, J. T. White, B. Maiorov, and A. T. Nelson, *Journal of*  
14 *nuclear materials* **498**, 438 (2018).
- 15 6 E. S. Wood, J. T. White, and A. T. Nelson, *Journal of Nuclear Materials* **484**, 245 (2017).
- 16 7 R. Harrison, C. Gasparrini, R. Worth, J. Buckley, M. Wenman, and T. Abram, *Corrosion*  
17 *Science* **174**, 108822 (2020).
- 18 8 T. Yan, D. Xie, Z. Chen, R. Yang, K. Zhu, C. Jiang, C. Ma, J. Liu, X. Wang, K. Liu, L. Luo, Q.  
19 Pan, and Y. Hu, *Journal of Nuclear Materials* **520**, 1 (2019).
- 20 9 A. Mohamad, B. Gong, T. Yao, A. R. Wagner, M. T. Benson, and J. Lian, *Journal of Nuclear*  
21 *Materials* **544**, 152691 (2021).
- 22 10 A. Mohamad, T. Yao, B. Gong, J. Harp, A. R. Wagner, A. T. Nelson, and J. Lian, *Journal of*  
23 *Alloys Compounds* **853**, 157319 (2021).
- 24 11 E. S. Wood, J. T. White, and A. T. Nelson, *Journal of Nuclear Materials* **489**, 84 (2017).
- 25 12 E. S. Wood, J. T. White, C. J. Grote, and A. T. Nelson, *Journal of Nuclear Materials* **501**,  
26 404 (2018).
- 27 13 A. T. Nelson, A. Migdisov, E. S. Wood, and C. J. Grote, *Journal of Nuclear Materials* **500**,  
28 81 (2018).
- 29 14 B. Gong, L. Cai, P. Lei, K. E. Metzger, E. J. Lahoda, F. A. Boylan, K. Yang, J. Fay, J. Harp,  
30 and J. Lian, *Corrosion Science* **177**, 109001 (2020).
- 31 15 I. Halikia, L. Zoumpoulakis, E. Christodoulou, and D. Prattis, *European Journal of Mineral*  
32 *Processing Environmental Protection* **1**, 89 (2001).
- 33 16 D. Shen, S. Gu, K. Luo, A. V. Bridgwater, and M. Fang, *Fuel* **88**, 1024 (2009).
- 34 17 L. Gašparovič, Z. Koreňová, and Ľ. Jelemenský, *Chemical papers* **64**, 174 (2010).
- 35 18 G. C. Silva, C. B. Yeamans, A. P. Sattelberger, T. Hartmann, G. S. Cerefice, and K. R.  
36 Czerwinski, *Inorganic chemistry* **48**, 10635 (2009).
- 37 19 K. Matusita and S. Sakka, *Journal of Non-Crystalline Solids* **38**, 741 (1980).
- 38 20 S. Aronson, R. Roof Jr, and J. Belle, *The Journal of Chemical Physics* **27**, 137 (1957).
- 39 21 A. Khawam and D. R. Flanagan, *Thermochimica Acta* **429**, 93 (2005).

1 22 M. Heydari, M. Rahman, and R. Gupta, International Journal of Chemical Engineering  
2 2015 (2015).  
3 23 J. M. Harp, P. A. Lessing, and R. E. Hoggan, Journal of Nuclear Materials **466**, 728 (2015).  
4 24 I. Halikia, P. Neou-Syngouna, and D. Kolitsa, Thermochemica Acta **320**, 75 (1998).  
5 25 A. A. Jain, A. Mehra, and V. V. Ranade, Fuel **165**, 490 (2016).  
6 26 L. Vlaev, I. Markovska, and L. Lyubchev, Thermochemica Acta **406**, 1 (2003).  
7 27 J. Orfao and F. Martins, Thermochemica Acta **390**, 195 (2002).  
8 28 J. Hancock and J. Sharp, Journal of the American Ceramic Society **55**, 74 (1972).  
9 29 J. Sharp, G. Brindley, and B. N. Achar, Journal of the American Ceramic Society **49**, 379  
10 (1966).  
11 30 M. Avrami, J. Chem. Phys. **7**, 1103 (1939).  
12 31 B. Erofe'ev, Compt Rend Acad Sci USSR **52**, 511 (1946).  
13 32 A. K. Galwey and M. E. Brown, *Thermal decomposition of ionic solids: chemical  
14 properties and reactivities of ionic crystalline phases* (Elsevier, 1999).  
15 33 S. Hasani, M. Panjepour, and M. Shamanian, Oxidation of metals **81**, 299 (2014).  
16 34 T. Ozawa, Bulletin of the chemical society of Japan **38**, 1881 (1965).  
17 35 J. H. Flynn and L. A. Wall, Journal of Polymer Science Part B: Polymer Letters **4**, 323  
18 (1966).  
19 36 H. L. Friedman, in *Kinetics of thermal degradation of char-forming plastics from  
20 thermogravimetry. Application to a phenolic plastic*, 1964 (Wiley Online Library), p. 183.  
21 37 T. Ozawa, Thermochemica acta **203**, 159 (1992).  
22 38 T. Akahira, Res. Rep. Chiba Inst. Technol. **16**, 22 (1971).  
23 39 W. A. JOHNSON and R. F. MEHL, Transactions **135**, 416 (1939).  
24 40 D. G. Boase and T. T. Vandergraaf, Nuclear Technology **32**, 60 (1977).  
25 41 R. J. McEachern and P. Taylor, Journal of Nuclear Materials **254**, 87 (1998).  
26 42 L. Quémard, L. Desgranges, V. Bouineau, M. Pijolat, G. Baldinozzi, N. Millot, J.-C. Nièpce,  
27 and A. Poulesquen, Journal of the European Ceramic Society **29**, 2791 (2009).  
28 43 A. K. Galwey and M. E. Brown, *Thermal decomposition of ionic solids: chemical  
29 properties and reactivities of ionic crystalline phases*, Vol. 86 (Elsevier, 1999).  
30 44 C. Gai, Z. Liu, G. Han, N. Peng, and A. Fan, Bioresource technology **181**, 148 (2015).  
31 45 S. S. Idris, N. Abd Rahman, and K. Ismail, Bioresource technology **123**, 581 (2012).  
32 46 L. Jiang, X. Yuan, H. Li, Z. Xiao, J. Liang, H. Wang, Z. Wu, X. Chen, and G. Zeng, Energy  
33 Conversion Management **106**, 282 (2015).  
34 47 D. Walker, Journal of Applied Chemistry **15**, 128 (1965).  
35 48 R. N. Worth, D. T. Goddard, J. Buckley, R. W. Harrison, H. Liu, J. I. Paul, and T. J. Abram,  
36 submitted to Journal of Nuclear Materials (2022).  
37 49 K. Johnson, V. Ström, J. Wallenius, and D. A. Lopes, Journal of Nuclear Science and  
38 Technology **54**, 280 (2017).  
39 50 T. Ohmichi and T. Honda, Journal of Nuclear Science Technology **5**, 600 (1968).  
40 51 R. McEachern, J. Choi, M. Kolar, W. Long, P. Taylor, and D. Wood, Journal of nuclear  
41 materials **249**, 58 (1997).  
42

43 **Figure Captions:**

1 **Figure 1:** A representative TGA data showing the normalized heat flow and weight change  
2 during the isothermal annealing of mc- and nc-U<sub>3</sub>Si<sub>2</sub> at 500 °C

3 **Figure 2:** XRD patterns of intermediate oxidation products for mc-U<sub>3</sub>Si<sub>2</sub> showing the formation  
4 of UO<sub>2</sub>, USi<sub>3</sub>, and U<sub>3</sub>O<sub>8</sub> during the oxidation process. The XRD patterns of U<sub>3</sub>Si<sub>2</sub>, UO<sub>2</sub> and U<sub>3</sub>O<sub>8</sub>  
5 were added for reference.

6 **Figure 3:** Plots of  $\ln [-\ln(1-\alpha)]$  versus  $\ln(t)$  of (A) mc-specimens and (B) nc-specimens showing  
7 great linearity, from which the characteristic factor  $n$  can be derived from the slope of each line,  
8 and the dominant reaction model can be revealed.

9 **Figure 4:** Plots of oxidation conversion as a function of time at three temperatures for (A) mc-  
10 specimens and (D) nc-specimens, linear relationship between  $g(\alpha)$  vs. time for (B) mc-specimens  
11 and (E) nc-specimens along with the slope  $k$  displayed near each line, and Arrhenius relationships  
12 between  $\ln k$  and  $1/T$  yielding activation energies,  $E_a$ , for (C) mc-specimens and (F) nc-specimens.

13 **Figure 5:** Plots of weight change during the non-isothermal oxidation of (A) mc-U<sub>3</sub>Si<sub>2</sub> and (B) nc-  
14 U<sub>3</sub>Si<sub>2</sub> with various heating rates. The oxidation onset temperature shifts to high values for nc-  
15 U<sub>3</sub>Si<sub>2</sub>.

16 **Figure 6:** Plots of  $\ln \beta$ ,  $\ln \left(\frac{\beta}{T^2}\right)$ , and  $\ln \frac{d\alpha}{dt}$  vs.  $1000/T$  for mc-U<sub>3</sub>Si<sub>2</sub> (A-C) and nc-U<sub>3</sub>Si<sub>2</sub> (D-F),  
17 corresponding to KAS, FWO, and Friedman methods, respectively. The activation energy  $E_a$  can  
18 be derived from the slope of each plot.

19

## 20 **Figure Captions:**

21 **Figure 1:** A representative TGA data showing the normalized heat flow and weight change  
22 during the isothermal annealing of mc- and nc-U<sub>3</sub>Si<sub>2</sub> at 500 °C

1 **Figure 2:** XRD patterns of intermediate oxidation products for mc-U<sub>3</sub>Si<sub>2</sub> showing the formation  
2 of UO<sub>2</sub> and U<sub>3</sub>O<sub>8</sub> during the oxidation process. The XRD patterns of UO<sub>2</sub> and U<sub>3</sub>O<sub>8</sub> were added  
3 for reference.

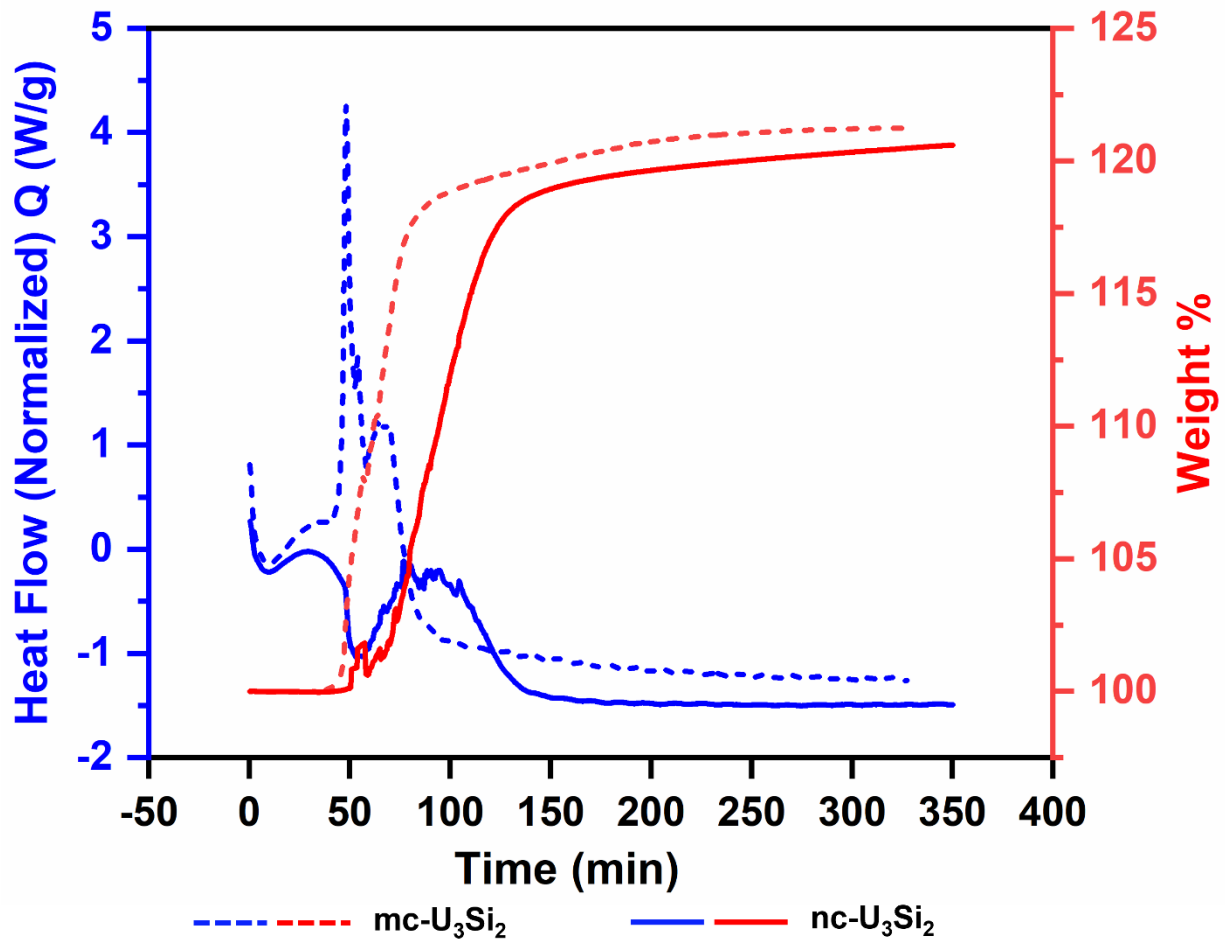
4 **Figure 3:** Plots of  $\ln [-\ln(1-\alpha)]$  versus  $\ln(t)$  of (A) mc-specimens and (B) nc-specimens showing  
5 great linearity, from which the characteristic factor  $n$  can be derived from the slope of each line,  
6 and the dominant reaction model can be revealed.

7 **Figure 4:** Plots of oxidation conversion as a function of time at three temperatures for (A) mc-  
8 specimens and (D) nc-specimens, linear relationship between  $g(\alpha)$  vs time for (B) mc-specimens  
9 and (E) nc-specimens along with the slope  $k$  displayed near each line, and Arrhenius relationships  
10 between  $\ln k$  and  $1/T$  yielding activation energies,  $E_a$ , for (C) mc-specimens and (F) nc-specimens.

11 **Figure 5:** Plots of weight change during the non-isothermal oxidation of (A) mc-U<sub>3</sub>Si<sub>2</sub> and (B) nc-  
12 U<sub>3</sub>Si<sub>2</sub> with various heating rates. The oxidation onset temperature shifts to high values for nc-  
13 U<sub>3</sub>Si<sub>2</sub>.

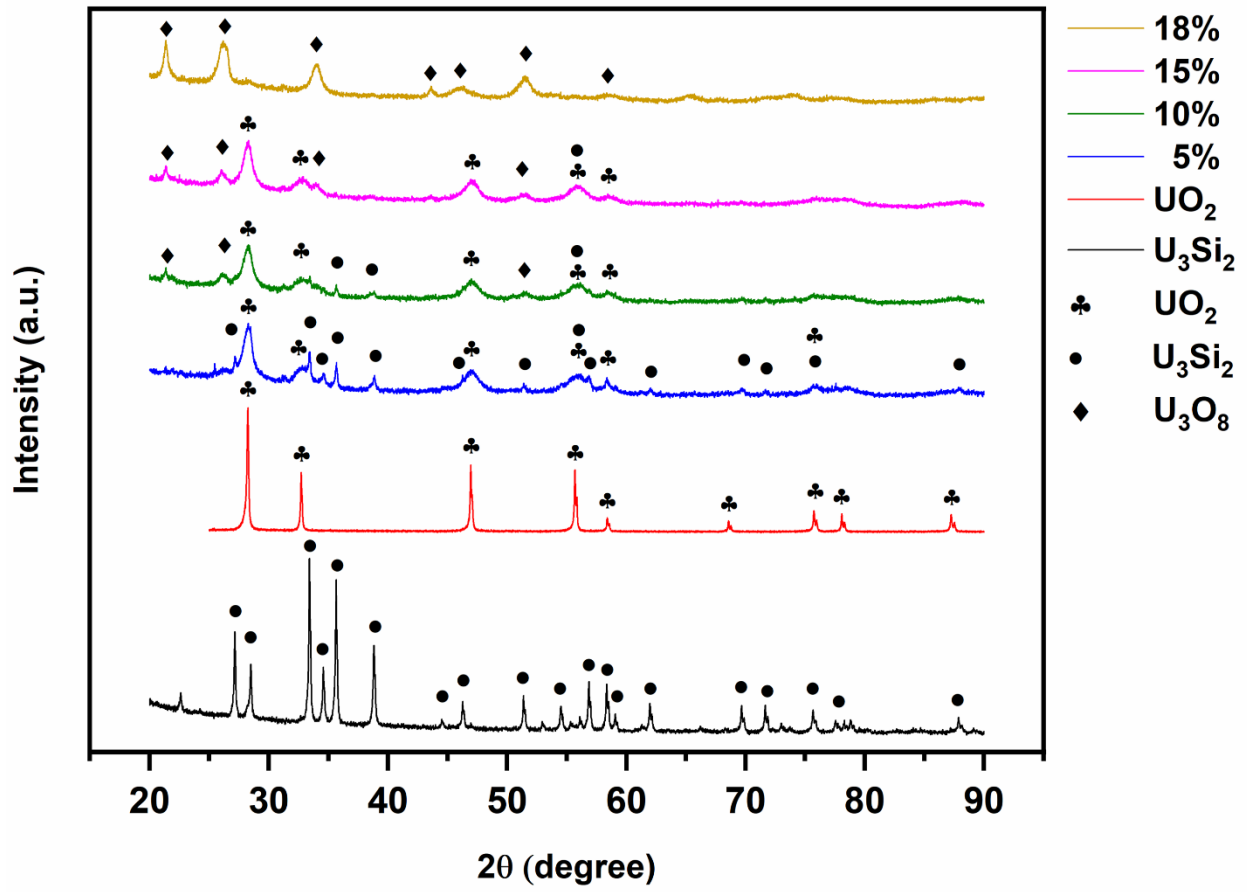
14 **Figure 6:** Plots of  $\ln \beta$ ,  $\ln \left(\frac{\beta}{T^2}\right)$ , and  $\ln \frac{d\alpha}{dt}$  vs.  $1000/T$  showing great linearity for mc-U<sub>3</sub>Si<sub>2</sub> (A-C)  
15 and nc-U<sub>3</sub>Si<sub>2</sub> (D-F), corresponding to KAS, FWO, and Friedman methods, respectively. The  
16 activation energy  $E_a$  can be derived from the slope of each plot.

17  
18



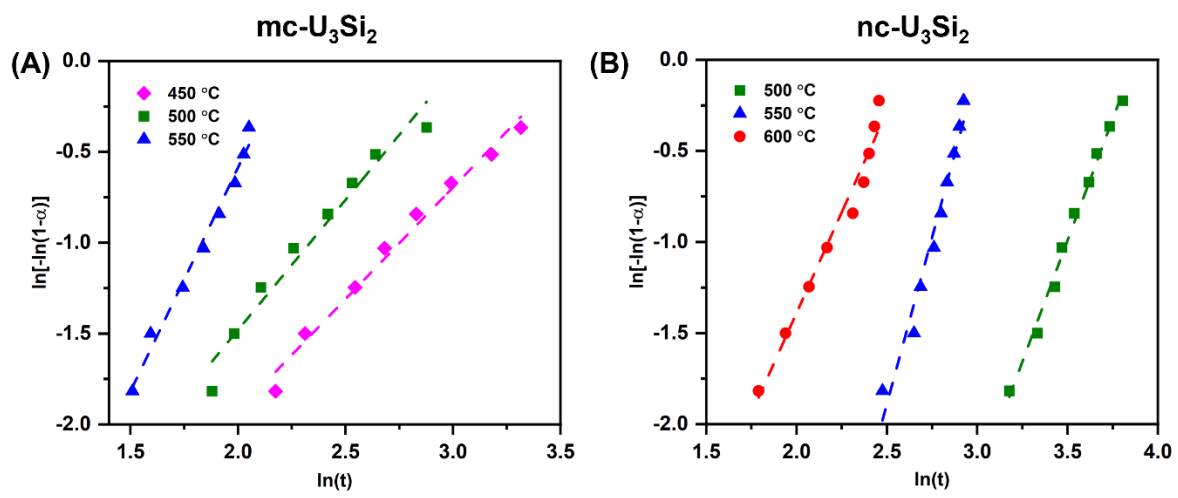
1  
2

Figure 1



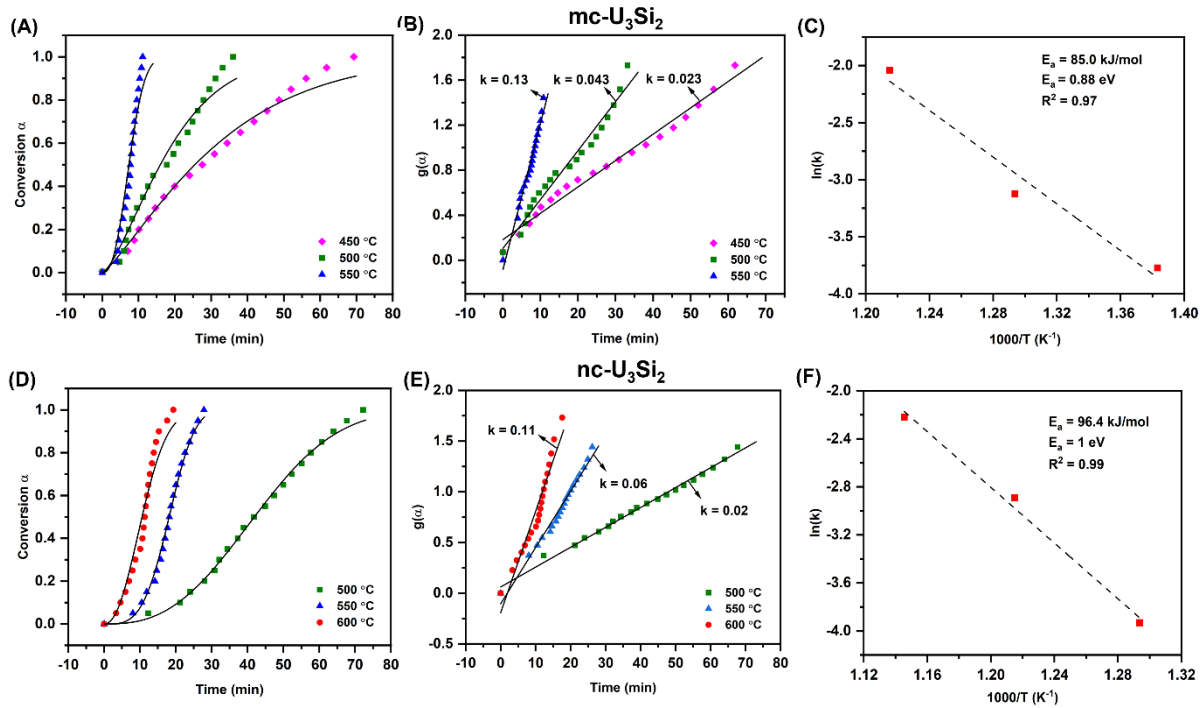
1  
2  
3

Figure 2



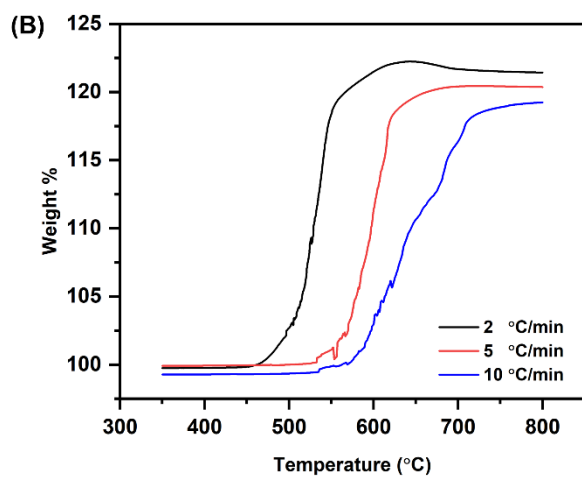
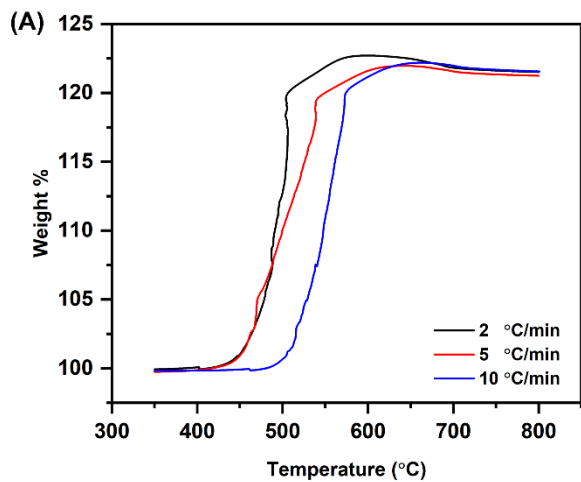
1  
2  
3  
4

Figure 3



1  
2  
3  
4  
5

Figure 4



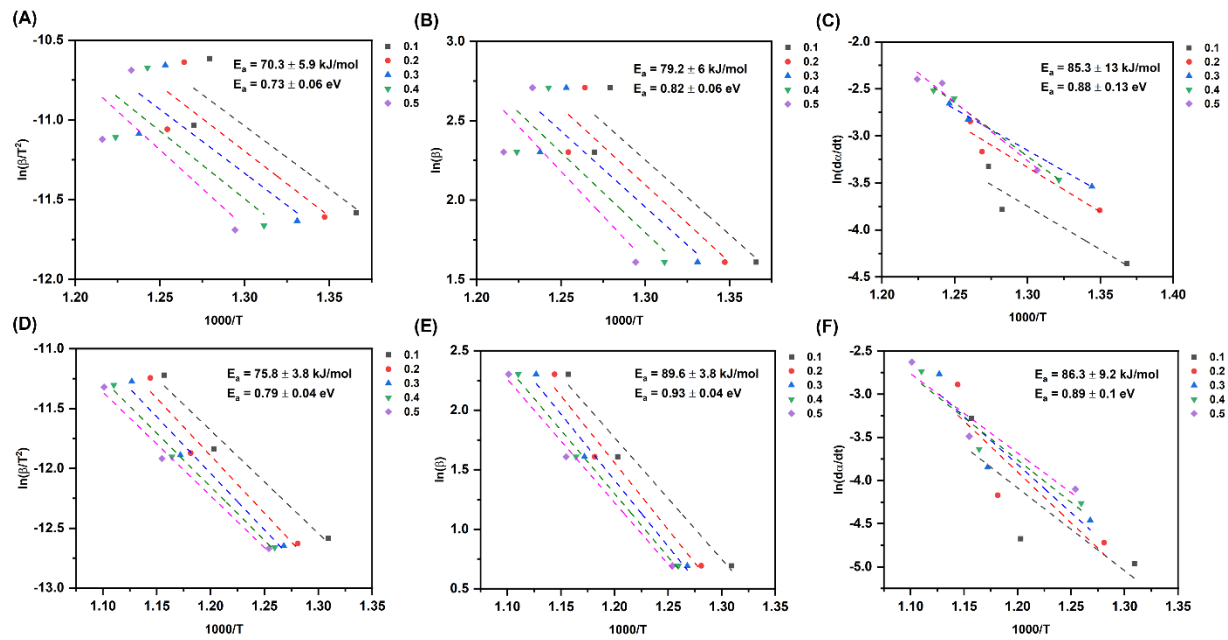
1

2

3

4

Figure 5



1

2

3

Figure 6